Research Article

Mingyang Tan, Yating Mao, and Travis W. Walker*

Rheological Enhancement of Artificial Sputum Medium

https://doi.org/10.1515/arh-2020-0100
Received May 27, 2019; accepted Mar 24, 2020

Abstract: This investigation proposes a synthetic biofluid, artificial sputum medium (ASM) and xanthan gum (XG), that mimics the mucus from a patient with cystic fibrosis, and investigates the rheological properties both macroscopically and microscopically. Macroscopic rheological characterization cannot address the heterogeneity or the behavior of particle transport inside the mucus. Microscopic rheology enables the characterization of the microenvironment by using microparticles as probes.
The addition of XG to ASM provides a tunable parameter that enables the mechanical properties to be consistent with real mucus. Particles that were suspended in a media of ASM with XG displayed a subdiffusive behavior at short timescales with a diffusive exponent that decreases with an increase in concentration of XG. At long timescales, particles that were suspended in ASM+XG with a concentration of XG of 0.1% to 0.4% displayed diffusive behavior. While in more concentrated samples (0.5% and 1.0%), the particles were constrained inside local elastic "cages". The microscopic moduli that were calculated showed consistently lower moduli than rotational rheometry. This discrepancy suggests that the solutions of XG have a hierarchical structure that better represents the weakly associated microstructure of mucus that is found in real sputum.

Keywords: microrheology; biofluid

1 Introduction

Mucus is a biological fluid that is found in the secretions of respiratory, gastrointestinal, urogenital, visual, and auditory systems of mammals, as well as the epidermis of amphibians, the gills of fish, and the external coating of snails and slugs. This complex fluid provides protection by humidifying and lubricating surfaces and by selectively enabling transport through a permeable film. At a macroscopic lengthscale (> 1 mm), mucus is often found to be a viscoelastic conglomeration that consists of water (≥ 95%), mucins (≥ 2%), salts, and cellular debris [1]. Mucins, the primary component of mucus that contributes up to 80% of the dry weight [2], are secreted by the goblet cells of the surface epithelium and by the mucous and serous cells of the submucosal glands [3]. The microstructure of mucus is formed primarily by the entanglement of these mucin fibers and other constituents of mucus [4], along with weaker non-covalent [5] and stronger disulfide bonds [6], creating a weak hydrogel.

Macroscopic (or bulk) rheological studies of mucus that use probing geometries on the order of centimeters have shown that its viscosity is usually very high at low shear rates, 10^4- to 10^6-times larger than the viscosity of water. At high shear rates near the physiological maximum, the viscosity of mucus was shown to decrease drastically to a value that is similar to the viscosity of water [6]. Chen et al. [7] used a double-tube capillary viscoelastometer to characterize the sputa of bronchitic patients, finding the viscosity to be 100 to 300 Pa·s, and the elastic modulus to be 1 to 2.5 Pa [8].

Compared with the macrorheology of mucus, studies of the microrheology have reported significantly different rheological properties. Since mucus has a heterogeneous micro-/nano-environment, nanoparticles have been shown to diffuse through the interstitial space that is surrounded by the microstructure of mucin at rates that are significantly higher than the predictions that are based on the macroscopic rheology. For instance, the Norwalk virus (*Norovirus*) with a size of 38 nm and the *human papillomavirus* (HPV) with a size of 55 nm were found to have the same rate of diffusion in human cervical mucus and

***Corresponding Author: Travis W. Walker:** Department of Chemical and Biological Engineering, South Dakota School of Mines & Technology, Rapid City, SD 57701, United States of America; Email: travis.walker@sdsmt.edu
Mingyang Tan: Department of Chemical and Biological Engineering, South Dakota School of Mines & Technology, Rapid City, SD 57701, United States of America
Yating Mao: School of Chemical, Biological, and Environmental Engineering, Oregon State University, Corvallis, OR 97331, United States of America

Open Access. © 2020 M. Tan *et al.*, published by De Gruyter. CC BY This work is licensed under the Creative Commons Attribution 4.0 License

in water, while the herpes simplex virus (HSV) with a size of 180 nm was found to have at least a 100- to 1,000-fold reduction in the rate of diffusion in mucus when compared with the rate of diffusion in water [9]. These observations imply that the microrheology of mucus depends on the lengthscale of the measurement, meaning that a particle whose size is larger than the lengthscale of the microstructure may experience steric obstruction in mucus while a particle whose size is smaller than the lengthscale of the microstructure is able to diffuse freely inside the void space of the microstructures. When the size of particles are about the same with the lengthscale of the microstructure, particles have been found to be able to jump between microstructures [10], which was also observed in this study.

Another important factor that has been shown to affect the measurement of microrheology is the surface properties of the probing particle. For instance, particles of polystyrene with a diameter of 200 nm that were coated with low-molecular-weight polyethylene glycol, a chemical group that prevents adhesion to the microstructure of mucin, were found to diffuse through sputum from a patient of cystic fibrosis 90-times faster than the uncoated particles of polystyrene of the same size. While the bulk viscosity was characterized to be 20,000-times greater than water, the viscosity at the microscale that was experienced by the coated particles was found to be only 5-times greater than the viscosity of water [11].

Cystic Fibrosis

Cystic fibrosis (CF) is a genetic disease that is caused by mutations in the cystic fibrosis transmembrane conductance regulator (CFTR) gene, which leads to an improper regulation of ions and to reduced water content [12]. The respiratory mucus of CF patients has unusually high rheological properties, resulting in the obstruction of mucociliary clearance, the colonization of bacteria, and finally severe infection [13, 14], which is exacerbated by difficulty of delivering antibiotics to the infected site or genetic medicine to the epithelium.

The transport of particles to the underlying tissue is largely hindered by the microstructure of the mucus, which presents rheologically at the macroscopic scale as a high viscoelastic modulus. However, detailed characterization of the viscoelastic properties of CF mucus at a microscopic lengthscale should promote the development of efficient drug-delivery vehicles. By probing with 100-nm and 200-nm particles, Dawson et al. [15] found that the viscosity of CF sputum at the microscale was at least an order of magnitude lower than the macroscopic viscosity that was measured by a cone-and-plate rheometer. Using the data from Dawson et al., we compared the macroscopic and microscopic rheological properties of CF sputum, as shown in Figure 1. The microscopic modulus is calculated by using the mean-squared displacement (MSD) data of Figure 2c of Dawson's paper. The discrepancy in diffusivity and subsequent rheology between the macroscopic rheology and the microscopic rheology increased to more than two orders of magnitude as the particle size decreased to 100 nm. Thus, the range in the rates of particle transport indicated that the mesh size of the CF sputum was not homogeneous.

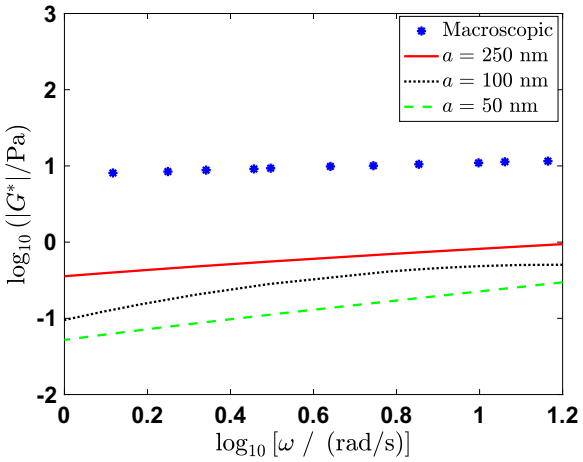

Figure 1: Comparison of $|G^*|$ between macroscopic and microscopic rheology from Dawson et al. [15]. A torsional rheometer with cone-and-plate geometry was used. Multiple particle tracking was used for the microrheology.

Interestingly, some researchers have shown that nanoparticles can diffuse more easily through CF sputum with a higher viscoelastic modulus [16]. The authors hypothesized that an increased viscoelastic moduli indicated an increase in biopolymer concentration and a subsequent increase in the number of junctions between the biopolymer chains. Further, they theorized that this structural change in the biological hydrogel could lead to local phase separation in the microstructural environment, which resulted in porous voids that provided paths for decreased resistance to diffusion.

These documented observations provide evidence for the need to design drug-delivery vehicles that are engineered to efficiently navigate the microstructure. Unfortunately, samples of CF sputum that are obtained from the pulmonary system of patients are difficult to obtain. The invasive collection of CF sputum can be harmful to the donors, while noninvasive methods of collection can result in contamination of the sample or in altering of the

microstructure. To enable continued research into techniques of delivery while overcoming this inaccessibility of CF sputum, this study investigated a recipe for a synthetic biofluid that had consistent rheological properties of pulmonary mucus from a patient with CF.

Synthetic Biofluids

For conducting a variety of research activities, synthetic biofluids provide a cheaper and less-invasive alternative to real biofluids. However, consistency of critical mechanical properties between the synthetic biofluids and the real biofluids is essential for properly staging a number of biophysical processes.

A variety of recipes for synthetic mucus can be found in the literature. To mimic tracheal mucus, Hamed et al. [17] used pig gastric mucin (PGM) type III and a solution of albumin with glutaraldehyde as a cross-linking agent to tune the viscoelasticity of the synthetic fluid. Hassan et al. [18] crosslinked locust bean gum (LBG) solution with Borax of two concentrations to make liquid-like mucus and solid-like mucus. However, since actual mucus is composed primarily of entangled fibers of mucin with associative bonds instead of cross-linked polymers, mucus will recover rapidly and reversibly upon shear [4, Chapter 4]. Schenck et al. [19] used Carbopol (manufactured by Lubrizol) poly(acrylic acid) to create hydrogels that mimic lung mucus. Dynamic oscillatory shear tests show that both elastic and viscous moduli have a sharp increase at a frequency of 10 rad/s. This erratic behavior indicates that the structure of the gel degrades at a high frequency, which is inconsistent with CF sputum. Sriramulu et al. [20] made artificial sputum medium (ASM) to emulate CF mucus. In Sriramulu's study, ASM served as a growth medium for *Pseudomonas aeruginosa* to simulate the infected status of CF mucus [20]. However, the viscoelastic moduli of ASM can easily be shown to be 3- to 4-orders of magnitude lower than the viscoelastic moduli of the real CF sputum that was reported by Dawson et al. [15].

In this study we investigated both the macroscopic and the microscopic rheological properties of an enhanced recipe of ASM that included varying concentrations of xanthan gum (XG), an exocellular heteropolysaccharide that is produced by the bacterium, *Xanthomonas campestris*. The conformation of xanthan gum in solution depends on the salt concentration and temperature. At low salt concentrations and high temperatures, the xanthan gum has a disordered form with a single-stranded structure [21–25]. Cations can shield the polymer from unfolding into a random coil, stabilizing the conformation in its double-stranded structure [26–32]. The goal of this study was to develop a standardized protocol for creating a cheap synthetic biofluid for CF sputum that is rheologically consistent at both the macroscopic and the microscopic length-scales.

Materials and Experimental Methods

ASM+XG

Solutions of ASM were made by the method that was discussed by following Sriramulu et al. [20], which is reproduced in Table 1. All of the ingredients except egg yolk emulsion were dissolved in DI water and then autoclaved for 30 minutes. After the solution cooled to room temperature, the egg yolk emulsion was added.

Xanthan gum (T622, CP Kelco) in powdered form was added into ASM with concentrations of 0.1%, 0.2%, 0.3%, 0.4%, 0.5%, and 1.0% to make the solutions of ASM+XG. These solutions were mixed thoroughly until the powder was dissolved.

Table 1: The ingredients of ASM. Adapted from [20].

Ingredients of ASM	
porcin mucin	5 g
fish sperm DNA	4 g
casamino acid	5 g
NaCl	5 g
KCl	2.2 g
Tris	15 ml (1 M)
DTPA	15 ml (1 mM)
egg yolk emulsion	5 ml
DI water	1 l

Macrorheology

We performed the macroscopic rheological measurements by using a standard rotational rheometer (DHR-3, TA Instruments) with a 2°, 40-mm stainless steel cone-and-plate geometry. We completed dynamic oscillatory strain sweeps at a frequency of $\omega_0 = 0.16$ rad/s for strains of $\gamma \in [10^{-4}, 0.5]$. The linear viscoelastic region was found to be below 10% deformation ($\gamma < 0.1$), and all subsequent frequency sweeps were completed at a strain of $\gamma_0 = 0.01$. The frequency-dependent elastic modulus, G', and viscous modulus, G'', were found by perform-

ing an oscillatory shear sweep with frequencies of $\omega \in [0.01, 50]$, rad/s. Finally, the shear viscosity was found by completing steady-shear flow sweeps with shear rates of $\dot{\gamma} \in [0.01, 100]$, 1/s.

Microrheology

We utilized *video microscopy particle tracking* to investigate the microscopic rheological properties of the sample. Video microscopy particle tracking is commonly used because of its low cost and complexity. The spatial and temporal resolution of this technique is usually sufficient to extract rheological properties that are comparable with those measured by macroscopic techniques [37, 39]. The microscopic rheological experiments were conducted by suspending one-micron particles of polystyrene in the medium. These particles are surface modified with carboxylate groups, and they are functionalized to be yellow/green-fluorescent (F8823, Thermo Fisher). The medium was loaded into a micro-channel slide (Sticky Slide Luer, Ibidi) with both ends that are sealed. The thermal (Brownian) motion of the fluorescent microparticles was imaged with a 40×/0.6 NA objective using an inverted microscope (Eclipse Ti-S, Nikon). The transient positions of approximately 50 in-frame particles were captured for a total of 5,000 frames at 31 frames per second with a CCD camera (Guppy Pro 125B, Allied Vision).

To generate the trajectories of the particles from the video, we followed the algorithm that was developed by Crocker and Grier [33]. The mean-squared displacement of each particle, $\Delta r^2(\tau)$, can be constructed from the respective trajectories. For a time step of size τ, the ensemble-averaged MSD is defined to be

$$\left\langle \Delta r^2(\tau; t) \right\rangle = \frac{1}{N} \sum_{i=1}^{N} \left[\mathbf{x}_i(t+\tau) - \mathbf{x}_i(t) \right]^2, \tag{1}$$

where N is the total number of particles, $\mathbf{x}_i$ is the position vector of particle i, which is projected to a two-dimensional plane in this study, and t is the global time. The time step size τ means that in a given measurement τ is chosen to be any fragment of the time of that measurement. So, τ is all possible time steps chosen from any two time points, as long as the step is chosen not to correlate with other chosen ones. In a Newtonian fluid, the MSD in the two-dimensional plane is related to the diffusivity such that

$$\left\langle \Delta r^2(\tau) \right\rangle = 4D\tau, \tag{2}$$

where D is the diffusivity (also known as the diffusion coefficient). The diffusivity can be found by the Stokes-Einstein relation,

$$D = \frac{k_B T}{6\pi\eta a}, \tag{3}$$

where k_B is the Boltzmann constant, T is the temperature, η is viscosity of the fluid, and a is the radius of the particle.

Mason and Weitz [34] proposed a generalized Stokes-Einstein relation (GSER) for particles that are suspended in a non-Newtonian fluid. The MSD in the reciprocal (frequency) space, $\left\langle \Delta\tilde{r}^2(\omega) \right\rangle$, is given by

$$\left\langle \Delta\tilde{r}^2(\omega) \right\rangle \approx \frac{2k_B T}{3\pi a i\omega \tilde{G}(\omega)}, \tag{4}$$

where ω is the frequency, i is the complex variable, and $\tilde{G}(\omega)$ is the complex modulus in the reciprocal space. The MSD can be expanded locally at a frequency of interest, ω_0, using a model power-law relation such that

$$\left\langle \Delta r^2(\tau; \omega_0) \right\rangle = \left\langle \Delta r^2(\omega_0) \right\rangle [\omega_0 t]^{\alpha(\omega_0)}, \tag{5}$$

where α is the diffusive exponent [35]. When a particle diffuses in a Newtonian fluid, the diffusion process is typical, and the diffusive exponent is unity, $\alpha = 1$. When the particle is trapped inside a Hookean solid, diffusion is suppressed, and the diffusive exponent is null, $\alpha = 0$. Thus, a particle exhibits subdiffusive behavior, $0 < \alpha < 1$, when it is suspended in a viscoelastic fluid that exhibits both liquid-like and solid-like mechanical properties. Using a Fourier transform [37, Chapter 3], the complex modulus in the reciprocal space can be found to be

$$\tilde{G}(\omega_0) = \frac{2k_B T}{3\pi a \langle \Delta r^2(t_0) \rangle \Gamma[1+\alpha(\omega_0)]} \exp\left[\frac{i\pi\alpha(\omega_0)}{2} \right], \tag{6}$$

where Γ is the gamma function. The elastic modulus, $\tilde{G}'$, is the real part of the complex modulus, and the viscous modulus, $\tilde{G}''$, is the imaginary part.

Errors that are associated with the experiments include the static error, δ, which is the intrinsic error of the system that is caused by factors such as the vibration of the setup, and the dynamic error, which is caused by the finite acquisition time, σ, of the image [35]. The position that is acquired at a certain time includes the history of the successive positions of the particle during the time interval that the shutter of the camera is open. Thus, we characterized the static error in the typical way by fixing particles in an agarose gel and measuring the subsequent MSD. The dynamic error was minimized by choosing a small shutter time, while ensuring that the particles were visible. The microscopic rheological measurements in this study were calibrated by measuring Newtonian fluids (water and glycerol solutions of different concentrations) and comparing with measurements by standard commercial rotational rheometer.

Table 2: Macroscopic and microscopic data of ASM, ASM+XG, and CF sputum [15].

ASM+XG	Macroscopic Rheology (ω = 1rad/s, γ_0 = 0.01)				Microscopic Rheology		
[% XG]	G' [Pa]	G'' [Pa]	ω_c [rad/s]	η_0 [Pa·s]	α [-]	t_r [s]	l_c [μm]
0%	6.5×10^{-4}	1.5×10^{-3}	––	––	1	∞	––
0.1%	0.14	0.11	0.62	0.55	0.68	1.1	0.19
0.2%	0.39	0.40	2.6	2.5	0.25	4.6	0.068
0.3%	1.2	0.86	11	11	0.22	5.8	0.050
0.4%	3.2	1.6	49	47	0.19	7.9	0.043
0.5%	5.1	2.2	––	78	0	––	0.027
1.0%	23	2.2	––	4×10^2	0	––	0.017
CF	7.3	2.2	––	51	––	––	––

Results and Discussion

The rheological properties of ASM+XG are tailored by using different concentrations of XG, and they are compared with the properties of CF sputum at the macroscopic lengthscale. The microscopic rheology focuses on the change in MSD and on the dependence of the relaxation time, the cage size, and the diffusive exponent on XG concentrations. A compilation of the macroscopic and microscopic rheological data can be found in Table 2.

Macroscopic Rheology

The macroscopic rheology of solutions of ASM and XG with different concentrations of XG were studied using a commercial rotational rheometer. Strain-sweep, frequency-sweep, and flow-sweep tests (Figures 2a-2c) were conducted to characterize the linear region of the samples, the frequency-dependent moduli, and steady-shear viscosities respectively. The errors associated with the limit of the instrument were co-plotted, according to the method that are proposed by Ewoldt et al. [38], to display the trust-worthy region of measurements. The strain-sweep and flow-sweep measurements are within the limit of the instrument. The dynamic oscillatory strain-sweep (Figure 2a) and frequency-sweep (Figure 2b) tests showed that the ASM+XG mixtures became more elastically dominated with an increase in concentration of XG. The crossover frequency decreased with increasing concentration of XG from 0.1% to 0.4%. For 0.5% to 1.0%, the elastic modulus dominated over all frequencies. The steady-shear tests showed that ASM+XG mixtures were shear thinning, as expected for many polymer solutions.

A comparison with data of CF sputum from Dawson et al. [15] in Figure 3 has shown that the enhancement of ASM by the addition of XG at a concentration of 0.5% created a synthetic biofluid with rheological properties that agreed well with the rheological properties of CF sputum. Figure 3 also shows plots of the elastic modulus, the viscous modulus, and the viscosity of pure ASM, which were approximately two orders of magnitude smaller than the values of CF sputum in all three cases.

Microscopic Rheology

The microscopic rheological results show that particles that are suspended in ASM have dramatically different behaviors depending on the concentration of XG (Figure 4). The random trajectory of particles in ASM with no addition of XG demonstrated a purely diffusive motion (Figure 4a), which is indicative of a viscous, inelastic material. The MSD of purely diffusive motion scales as t^1, as exemplified in Figure 5. The viscosity of ASM that was obtained by using the Stokes-Einstein relation was found to be 1.6×10^{-3} Pa·s. Although ASM consists of some macromolecules (porcine mucin, fish DNA, etc. [20]), the concentrations of these materials are too low to exhibit any elastic contributions. When XG was added to ASM, the thermal motion of the particles were altered. As shown in Figures 4b-(c), particles that were diffusing in samples of ASM with the addition of 0.1% and 0.2% of XG displayed two regions of dynamics. At short times the particle were constrained inside an elastic "cage", where a blob of trajectories can be seen. At long times the particles "hopped" from one elastic cage into another elastic cage, which can be seen in the trajectories as "blobs" that are connected to each other. As the concentration of XG in ASM was increased, the size of the blobs became smaller in size and more dense in trajectories, and the paths that connect the blobs became shorter. As shown in Figure 4d, in a concen-

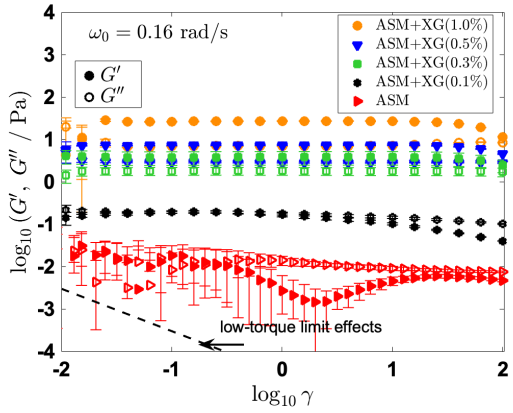

(a) Strain sweep

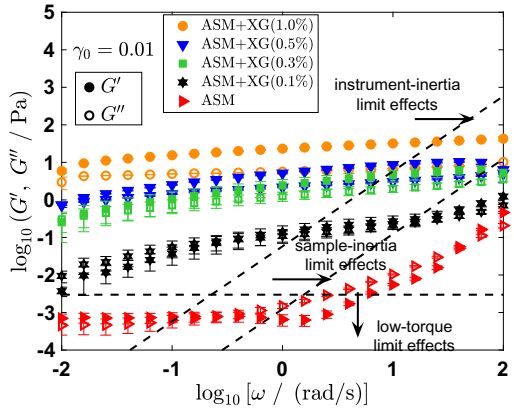

(b) Frequency sweep

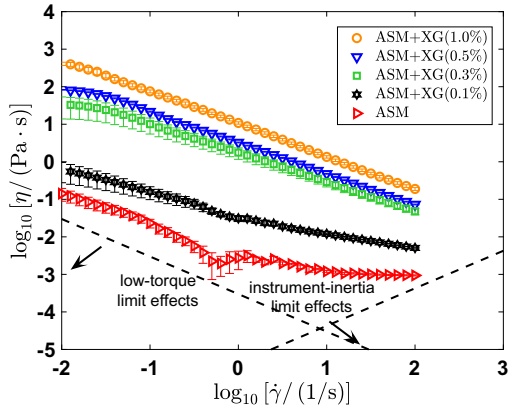

(c) Flow sweep

Figure 2: Rheology of ASM+XG for different concentrations of XG, $C_{\mathrm{XG}} \in \{0.1, 0.3, 0.5, 1.0\}\%$. (a) The strain-dependent elastic modulus (G', closed symbols) and viscous modulus (G'', open symbols). Strain sweeps were completed at a frequency $\omega_0 = 0.16$ rad/s. (b) The frequency-dependent elastic modulus (G', closed symbols) and viscous modulus (G'', open symbols). Frequency sweeps were completed at a strain of $\gamma_0 = 0.01$. (c) The apparent shear viscosities as a function of shear rate.

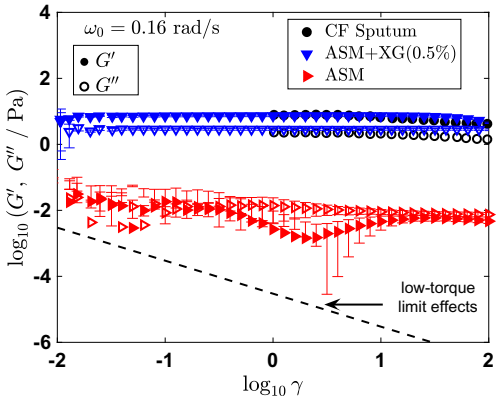

(a) Strain sweep

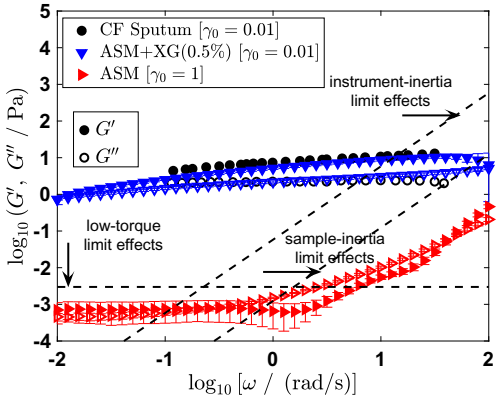

(b) Frequency sweep

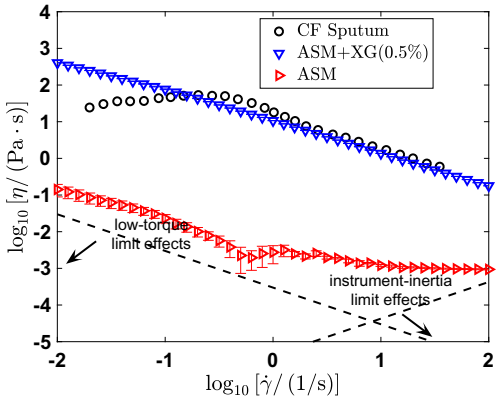

(c) Flow sweep

Figure 3: Comparison of rheological properties of ASM and ASM+XG(0.5%) to CF sputum from Dawon et al. [15]. (a) The strain-dependent elastic modulus (G', closed symbols) and viscous modulus (G'', open symbols). Strain sweeps were completed at a frequency $\omega_0 = 1$ rad/s. (b) The frequency-dependent elastic modulus (G', closed symbols) and viscous modulus (G'', open symbols). Frequency sweeps were completed at a strain of $\gamma_0 = 0.01$ for CF sputum and ASM+XG and at a strain of $\gamma_0 = 1.0$ for ASM. (c) The apparent shear viscosities as a function of shear rate.

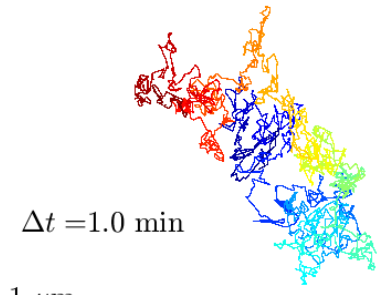

(a) ASM

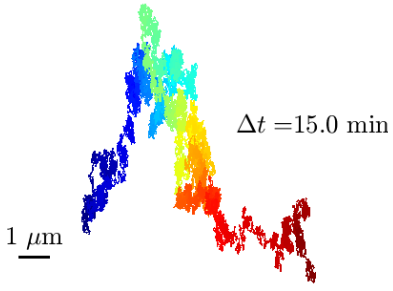

(b) ASM+XG(0.1%)

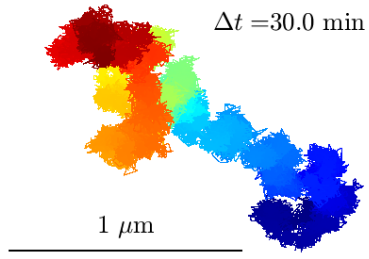

(c) ASM+XG(0.2%)

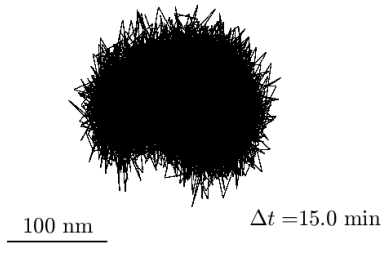

(d) ASM+XG(1.0%)

Figure 4: Trajectories of a single 1-μm particle. (a) In ASM, the particle is diffusive, traveling over 10 μm in 1.0 min. (b) In ASM+XG(0.1%), the particle is subdiffusive at short times, but the particle is diffusive at long times, traveling over 10 μm in 15.0 min. (c) In ASM+XG(0.2%), again, the particle is subdiffusive at short times, and the particle is diffusve at long times, traveling over 1 μm in 30.0 min. (d) In ASM+XG(1.0%), the particle is no longer diffusive, as the particle only samples its local environment of $\sim$ 200 nm in 15.0 min.

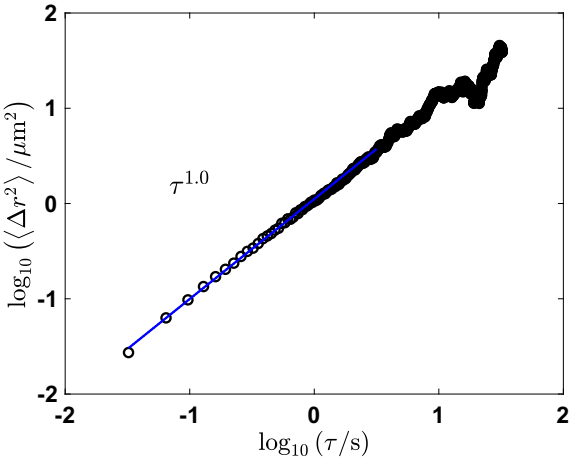

Figure 5: MSD of particles that were suspended in ASM. The MSD scales as t^1, and the viscosity was measured to be 1.6×10^{-3} Pa·s.

tration of 1.0%, the particles were not able to diffuse, and they became trapped in a single environment.

Particles that are suspended in a more concentrated mixture of XG in ASM needed to expend more energy to escape the cages. The hopping behavior can also be seen in the plots of MSD versus time (Figure 6(a)-(b)). A typical curve of MSD versus time for a Newtonian fluid (such as AM) is shown in Figure 5. When XG was added to the ASM, the diffusive exponent was less than one at short times, when the particles were constrained inside the elastic cage, and they exhibited subdiffusive motion. At long times when the particles escaped their current cage and moved to their next cage, their overall motion again became random, resulting in an overall diffusive motion. The intersection of the subdiffusive region and the diffusive region indicated a characteristic relaxation time, t_r, of the polymer and a characteristic cage size, ℓ_c. As shown in Figure 6 and plotted explicitly in Figure 7, as the concentration of XG (C_{XG}) was increased, the relaxation time increased, scaling as $C_{\mathrm{XG}}^{1.40}$, and the cage size decreased, scaling as $C_{\mathrm{XG}}^{-2.07}$.

When the concentration of XG was increased above 0.4% to 0.5%, the particles appeared to become permanently constrained inside the elastic cage, and the resulting diffusive exponent became approximately zero. This general trend in constrained motion as a function of concentration of XG can be seen in Figure 7c, where the diffusive exponent decreased with an increase of the concentration of XG. The transition of the motion of the particles from diffusing in a viscous fluid to being constrained in an elastic gel can be seen in Figure 8. The diffusive exponent changes from 1 to 0 as the concentration of XG was increased to 0.5%.

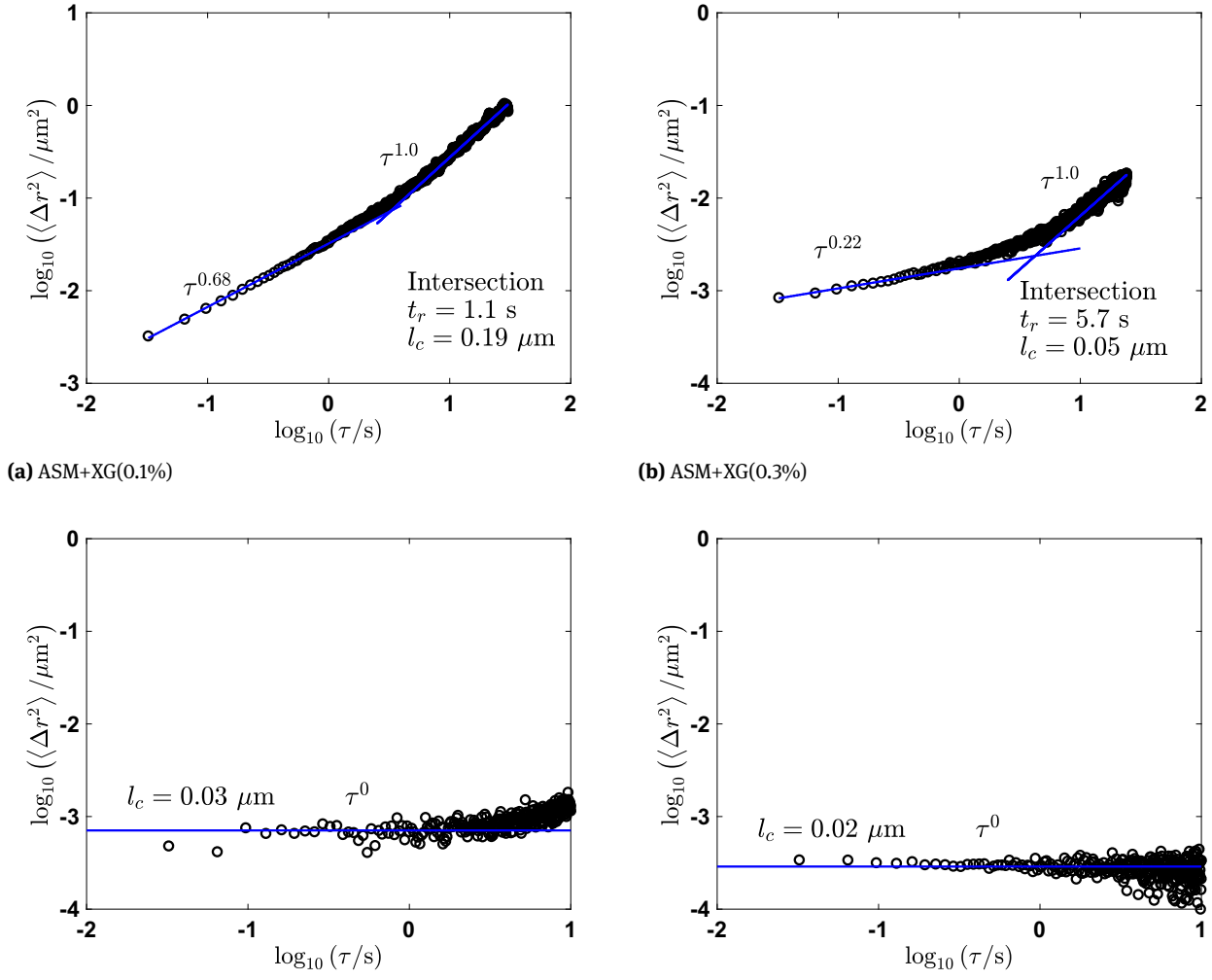

(a) ASM+XG(0.1%)

(b) ASM+XG(0.3%)

(c) ASM+XG(0.5%)

(d) ASM+XG(1.0%)

Figure 6: MSD of particles that were suspended in ASM at varying concentrations of XG, $C_{XG} \in \{0.1, 0.3, 0.5, 1.0\}$%. (a) The intersection of subdiffusion and diffusion is at $(t_r, \ell_c) = (1.1\text{ s}, 0.19\ \mu\text{m})$. (b) The intersection of subdiffusion and diffusion is at $(t_r, \ell_c) = (5.7\text{ s}, 0.05\ \mu\text{m})$. (c) The MSD scales as τ^0, and $\ell_c = 0.03\ \mu$m. (d) The MSD scales as τ^0, and $\ell_c = 0.02\ \mu$m. With an increase of the concentration of XG, the motion of the particles become more subdiffusive, the relaxation time becomes longer, and the cage size becomes smaller. Ultimately, the particles are bounded inside elastic cages at the concentrations of 0.5% and 1.0%, where the motion implies that the media was a viscoelastic solid.

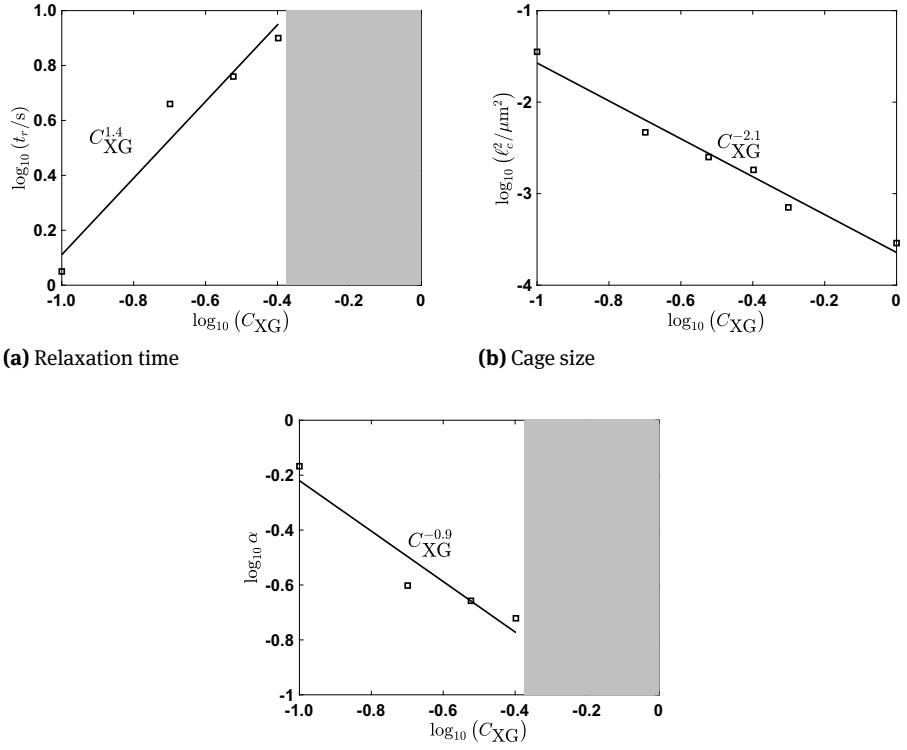

(a) Relaxation time **(b)** Cage size

(c) Diffusive exponent

Figure 7: Diffusive properties as a function of the concentration of XG. (a) The relaxation time t_r versus concentration. The relaxation time increases with the concentration of XG with the scaling of $C_{\mathrm{XG}}^{1.4}$. The gray area shows that, at a concentration of 0.5% and higher, the particles are permanently captured in elastic cages, and the relaxation time cannot be obtained. (b) The cage size ℓ_c versus concentration. The cage size decreases with the concentration of XG with the scaling of $C_{\mathrm{XG}}^{-2.07}$. (c) The diffusive exponent α versus concentration. With an increase of the concentration of XG (from 0.1% to 0.4%), the motions of the particles become more subdiffusive, and the diffusive exponent, α, scales as $C_{\mathrm{XG}}^{-0.92}$. The gray area shows that, at a concentration of 0.5% and higher, the diffusive exponent is zero, and the ASM+XG mixtures are purely elastic.

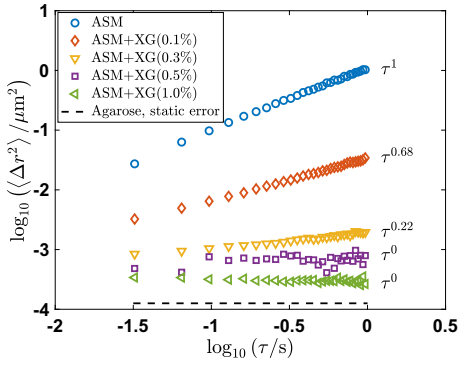

Figure 8: MSD of particles that were suspended in ASM with different concentrations of XG. The slope of MSD shows that the ASM is purely viscous $(\mathrm{MSD} \sim \tau^1)$. With an increase in concentration of XG, the mixture becomes elastically dominated, and eventually, it becomes a pure solid $(\mathrm{MSD} \sim \tau^0)$. The agarose that was used to characterize the static error of the experimental system is shown for comparison of the cage size.

From the same plots of MSD (Figure 6), the elastic and viscous moduli were obtained as a function of frequency by using the GSER. These values are compared with the bulk moduli that were obtained from standard rotational rheometry in Figure 9. The complex modulus is shown for samples of concentration of XG of 0.5% and 1.0%, as the microscopic rheological data did not provide a measurable viscous modulus. In Figure 9a-(b), the crossover frequency (ω_c, the reciprocal of the characteristic "relaxation" time) obtained from the microscopic rheological measurements generally decreased as the concentration of XG increased, which is in agreement with the macroscopic rheological measurements. However, the moduli that were obtained microscopically at high frequencies $(> 10\,\mathrm{rad/s})$ were consistently about one order of magnitude smaller than the moduli that were obtained macroscopically, which is consistent with the results from Dawson et al. in Figure 1 [15]. Thus, the solutions of XG appear

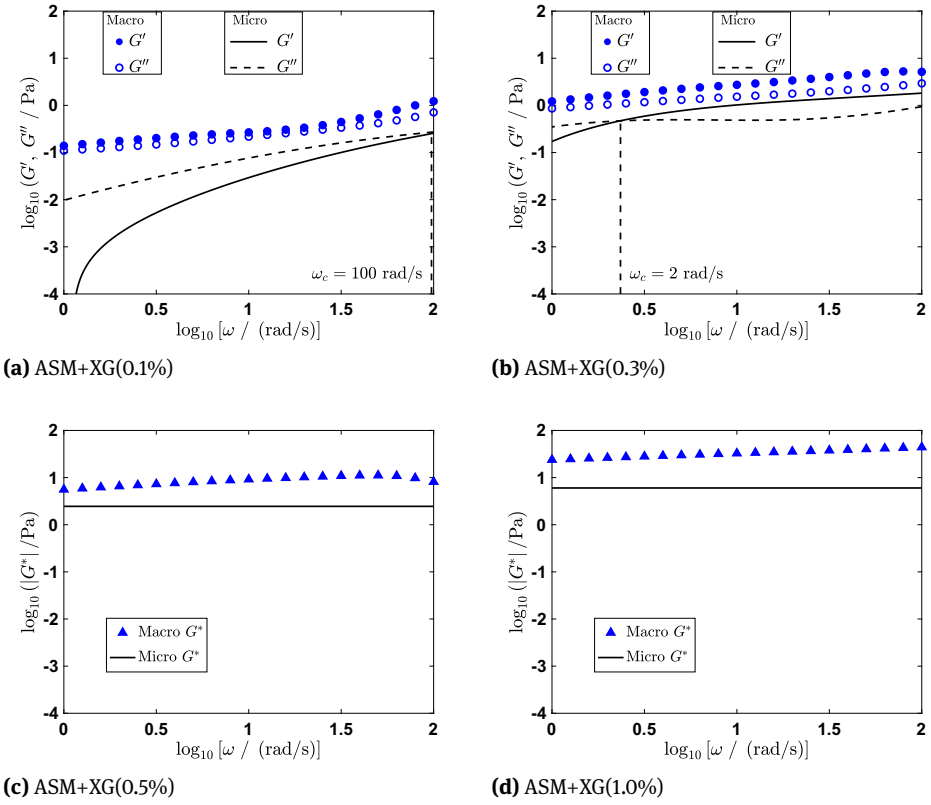

(a) ASM+XG(0.1%) **(b)** ASM+XG(0.3%)

(c) ASM+XG(0.5%) **(d)** ASM+XG(1.0%)

Figure 9: Comparison between microscopic rheology and macroscopic rheology for varying concentrations of XG. (a), (b) Elastic modulus G' and viscous modulus G'' for concentrations of XG of 0.1% and 0.3%. Lines are used for microscopic rheology, and spheres are used for macroscopic rheology. Solid lines or filled symbols are used for G' and dashed lines or open symbols are used for G''. (c), (d) Comparison of $|G^*|$ of concentrations of XG of 0.5% and 1.0%. Lines are used for microscopic rheology and triangular symbols are used for macroscopic rheology.

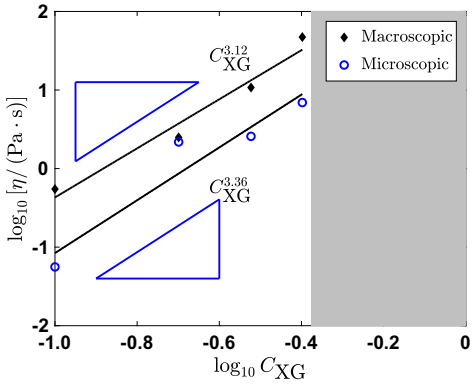

Figure 10: Viscosity of ASM as a function of different concentrations of XG, $C_{\text{XG}} \in \{0.1, 0.2, 0.3, 0.4\}$%. The gray area shows the concentration of XG that cannot be used to calculate the viscosity because the particles are permanently captured in elastic cages. The microscopic viscosities were obtained from the long-time diffusive region. The macroscopic viscosity was found using the zero-shear viscosity.

to have a hierarchy of structures that is similar to CF sputum.

These results can be described by considering that the particles could have been constrained inside a small first-order structure that was itself contained inside a larger second-order structure. Since the size of the particles may have been small when compared with the second- or higher-order structures, the rheological properties at higher order would not have been probed. The macroscopic rheological techniques, however, averaged the properties of the material at lengthscales that are greater than a millimeter. The viscosities that were obtained in this diffusive region at long times were compared with the zero-shear viscosities that were obtained from standard rotational rheometry. Figure 10 shows that the bulk viscosities were again consistently about an order of magnitude larger than the viscosities that were obtained from the microscopic rheological technique. However, the scale of the viscosity with concentration was close between the macroscopic and microscopic methods, which

is consistent with the theoretical scaling prediction from reptation theory ($\eta_0 \sim C_{XG}^{3.75}$) [36].

Conclusion

The rate of diffusion of 1-μm particles in ASM was found to be only 1.6-times slower than the diffusion rate in water. The low concentration of polymers in ASM had trivial influence on the elastic properties at a microscopic lengthscale. The addition of XG, however, created weakly-associated elastic cages that bounded the probe particles. The ionic environment of the ASM solution causes XG to conform to a fivefold helix, and the intermolecular associations cause the formation of networks, or elastic "cages" of XG. At lower concentrations ($C_{XG} \leq 0.4\%$), the particles were observed to escape the cages at long times. At higher concentrations ($C_{XG} \geq 0.5\%$), the resulting material appeared gel-like, and the particles were observed to be restrained inside the cages. This study provides preliminary microrheological data by using less costly materials and directs future studies, for instance, on the dependence of particle size and surface functionality. To study the discrepancy between macroscopic and microscopic rheology of ASM+XG, larger particles should be used.

Acknowledgement: The authors would like to thank Uranbileg Daalkhaijav, Annika Gabriel, Marisa Thierheimer, and Hope Wolterman for their help with developing the formulation. The authors would like to thank the Medical Research Foundation of Oregon for providing funding. This material is based upon work that was supported by the National Science Foundation under Grant Nos. 1652958 and 1842580.

References

[1] Chilvers M, O'callaghan C. Local mucociliary defence mechanisms. Paediatr Respir Rev. 2000;1(1):27–34. doi:10.1053/prrv.2000.0009.

[2] Masson P, Heremans J. Sputum proteins. Fundamentals and clinical pathology. Springfield: Charles C Thomas. 1973;412–474.

[3] Sturgess J, Palfrey ., Reid L. Rheological properties of sputum. Rheol Acta. 1971;10(1):36–43. doi:10.1007/bf01972474.

[4] Cone R. Mucus Immunology, Academic Press, San Diego, 1999.

[5] Carlstedt I, Sheehan J. Macromolecular properties and polymeric structure of mucus glycoproteins. Mucus and Mucosa. 1984;109:157–172. doi:10.1002/9780470720905.ch11.

[6] Meyer F, Silberberg A. The rheology and molecular organization of epithelial mucus. Biorheology. 1980;17(1):163–168. doi:10.3233/bir-1980-171-217.

[7] Chen T, Dulfano M. Mucus viscoelasticity and mucociliary transport rate. J Lab Clin Med. 1978; 91(3):423–431.

[8] Adler K, Dulfano M. The rheological factor in mucociliary clearance. J Lab Clin Med. 1976;88(1):22–28.

[9] Olmsted S, Padgett J, Yudin A, Whaley K, Moench T, Cone R. Diffusion of macromolecules and virus-like particles in human cervical mucus. Biophys J. 2001;81(4):1930–1937. doi:10.1016/s0006-3495(01)75844-4.

[10] Wong I, Gardel M, Reichman D, Weeks E, Valentine M, Bausch A, Weitz D. Anomalous diffusion probes microstructure dynamics of entangled F-actin networks. Phys Rev Lett. 2004;92(17):178101. doi:10.1103/physrevlett.92.178101.

[11] Suk JS, Lai SK, Wang Y, Ensign LM, Zeitlin PL, Boyle MP, Hanes J. The penetration of fresh undiluted sputum expectorated by cystic fibrosis patients by non-adhesive polymer nanoparticles. Biomaterials. 2009;30(13):2591–2597. doi:10.1016/j.biomaterials.2008.12.076.

[12] Rubin BK. Mucus structure and properties in cystic fibrosis. Paediatr Respir Rev. 2007;8(1):4–7. doi:10.1016/j.prrv.2007.02.004.

[13] Boucher RC, Cotton CU, Gatzy J, Knowles MR, Yankaskas JR. Evidence for reduced Cl-and increased Na+ permeability in cystic fibrosis human primary cell cultures.,The J Physiol. 1988;405(1):77–103. doi:10.1113/jphysiol.1988.sp017322.

[14] Smith JJ, Travis SM, Greenberg EP, Welsh MJ. Cystic fibrosis airway epithelia fail to kill bacteria because of abnormal airway surface fluid. Cell. 1996;85(2):229–236. doi:10.1016/s0092-8674(00)81099-5.

[15] Dawson M, Wirtz D, Hanes J. Enhanced viscoelasticity of human cystic fibrotic sputum correlates with increasing microheterogeneity in particle transport. J Biol Chem. 2003;278(50):50393–50401. doi:10.1074/jbc.m309026200.

[16] Sanders NN, De Smedt SC, Van Rompaey E, Simoens P, De Baets F, Demeester J. Cystic fibrosis sputum: a barrier to the transport of nanospheres. Am J Respir Crit Care Med. 2000;162(5):1905–1911. doi:10.1164/ajrccm.162.5.9909009.

[17] Hamed R, Fiegel J. Synthetic tracheal mucus with native rheological and surface tension properties. J Biomed Mater Res A. 2014;102(6):1788–1798. doi:10.1002/jbm.a.34851.

[18] Hassan A, Evrensel C, Krumpe P. Clearance of viscoelastic mucus simulant with airflow in a rectangular channel, an experimental study. Technol Health Care. 2006;14(1):1–11. doi:10.3233/thc-2006-14101.

[19] Schenck DM, Fiegel J. Tensiometric and phase domain behavior of lung surfactant on mucus-like viscoelastic hydrogels. ACS Appl Mater Interfaces. 2016;8(9):5917–5928. doi:10.1021/acsami.6b00294.

[20] Sriramulu DD, Lünsdorf H, Lam JS, Römling U. Microcolony formation: a novel biofilm model of *Pseudomonas aeruginosa* for the cystic fibrosis lung. J Med Microbiol. 2005;54(7):667–676. doi:10.1099/jmm.0.45969-0.

[21] Milas M, Rinaudo M. Properties of xanthan gum in aqueous solutions: role of the conformational transition. Carbohydr Res. 1986;158:191–204. doi:10.1016/0008-6215(86)84017-4.

[22] Norton IT, Goodall DM, Morris ER, Rees DA. Kinetic evidence for intramolecular conformational ordering of the extracellular polysaccharide (xanthan) from Xanthomonas campestris. J Chem Soc Chem Commun. 1980;(12):545–547. doi:10.1039/c39800000545.

[23] Lambert F, Milas M, Rinaudo M. Sodium and calcium counterion activity in the presence of xanthan polysaccharide. Int J Biol Macromol. 1985; 7(1):49–52. doi:10.1016/0141-8130(85)90066-2.

[24] Holzwarth G, Prestridge E. Multistranded helix in xanthan polysaccharide, Science, 1977, 197, 757–759.

[25] Rinaudo M., Milas M., Enzymic hydrolysis of the bacterial polysaccharide xanthan by cellulase. Int J Biol Macromol. 1980; 2(1):45–48. doi:10.1016/0141-8130(80)90009-4.

[26] Paoletti S, Cesàro A, Delben F. Thermally induced conformational transition of xanthan polyelectrolyte. Carbohydr Res. 1983;123(1):173–178. doi:10.1016/0008-6215(83)88394-3.

[27] Baradossi G, Brant D. Light scattering study of a series of xanthan fractions in aqueous solutions. Macromolecules. 1982;15(3):874–879. doi:10.1021/ma00231a035.

[28] Sato T, Norisuye T, Fujita H. Double-stranded helix of xanthan in dilute solution: evidence from light scattering. Polym J. 1984;16(4):341–350. doi:10.1295/polymj.16.341.

[29] Sato T, Norisuye T, Fujita H. Double-stranded helix of xanthan: dimensional and hydrodynamic properties in 0.1 M aqueous sodium chloride. Macromolecules. 1984;17(12): 2696–2700. doi:10.1021/ma00142a043.

[30] Stokke BT, Elgsaeter A, Smidsrod O. Electron microscopic study of single-and double-stranded xanthan. Int J Biol Macromol. 1986; 8(4):217–225. doi:10.1016/0141-8130(86)90030-9.

[31] Kitamura S, Takeo K, Kuge T, Stokke BT. Thermally induced conformational transition of double-stranded xanthan in aqueous salt solutions. Biopolymers. 1991;31(11):1243–1255. doi: 10.1002/bip.360311102.

[32] Lecourtier J, Chauveteau G, Muller G. Salt-induced extension and dissociation of a native double-stranded xanthan. Int J Biol Macromol. 1986;8(5):306–310. doi:10.1016/0141-8130(86)90045-0.

[33] Crocker JC, Grier DG. Methods of digital video microscopy for colloidal studies. J Colloid Interface Sci. 1996;179(1):298–310. doi:10.1006/jcis.1996.0217.

[34] Mason T, Weitz D. Optical measurements of frequency-dependent linear viscoelastic moduli of complex fluids. Phys Rev Lett. 1995;74(7):1250–1253. doi:10.1103/physrevlett.74.1250.

[35] Savin T, Doyle PS. Static and dynamic errors in particle tracking microrheology. Biophys J. 2005;88(1):623–638. doi:10.1529/biophysj.104.042457.

[36] DeGennes P. Dynamics of entangled polymer solutions. II. Inclusion of hydrodynamic interactions. Macromolecules. 1976;9(4):594–598. doi:10.1021/ma60052a012.

[37] Furst E, Squires T. Microrheology, Oxford University Press, New York, 2018.

[38] Ewoldt RH, Johnston MT, Caretta LM. Experimental challenges of shear rheology: how to avoid bad data. 2014;207–241. doi:10.1007/978-1-4939-2065-56.

[39] Savin T., Multiple particle tracking to assess the microstructure of biological fluids [dissertation]. Massachusetts Institute of Technology; 2006.